Soft Matter

Accepted Manuscript

This article can be cited before page numbers have been issued, to do this please use: B. Berteloot, I. Nys, G. Poy, J. Beeckman and K. Neyts, *Soft Matter*, 2020, DOI: 10.1039/D0SM00308E.

ROYAL SOCIETY OF CHEMISTRY

rsc.li/soft-matter-journal

View Article Online
DOI: 10.1039/D0SM00308E

Soft Matter

ARTICLE TYPE

Cite this: DOI: 00.0000/xxxxxxxxxx

Ring-shaped liquid crystal structures through patterned planar photo-alignment†

B. Berteloot,*[a] I. Nys*[a],G. Poy[b], J. Beeckman[a] and K. Neyts[a]

Received Date
Accepted Date

DOI: 00.0000/xxxxxxxxxx

Patterned liquid crystal (LC) configurations find widespread applications in functional devices such as lenses, gratings, displays and soft-robots. In combination with external stimuli such as an applied electric field, photo-alignment at the surfaces offers an attractive way to stabilize different LC structures in the bulk of a device. Herein, a planar LC cell is developed using a photo-alignment layer at the bottom substrate and a rubbed Nylon film at the top substrate. Patterned planar photo-alignment is achieved by modulating the linear polarization with a spatial light modulator (SLM) and projecting the pattern onto the bottom substrate. A ring pattern is written into the photo-alignment layer with a continuous rotation between an inner radius and an outer radius. In the other regions the alignment is parallel to the rubbing direction at the top substrate. Four different LC configurations are observed: structure A in which a ring-shaped region is formed with an out of plane (vertical) orientation perpendicular to the substrate, structure B which has a single disclination loop and a 180° twist at the inner region of the photo-patterned ring ($r < r_{in}$), structure C which has no discontinuities but a 360° twist in the inner region of the photo-patterned ring ($r < r_{in}$) and structure D with 2 disclination loops. The LC director configuration for all 4 structures is simulated through finite element (FE) Q-tensor simulations and the optical transmission for each structure is simulated using a generalized beam propagation method.

1 Introduction

Nematic liquid crystals (LC) are widely used in electronic displays (LCDs) and photonic applications, and the proper alignment of the LC director at solid interfaces is essential. Photo-alignment is a non-contact technique, that aligns the LC director perpendicularly to the plane of polarization of incident blue or UV light. Arbitrary patterned alignment orientations have been demonstrated at sub-micrometer resolution.[1–4] The most common approach uses interference of two circularly polarized laser beams with opposite handedness.[5,6] The second approach uses a direct-write setup in which a polarization modulator (Pockels cell) is used to rapidly rotate the polarization plane of the laser while moving the sample with an XY-translation stage.[7,8] A third (sometimes called holographic) approach is based on the projection of a spatial light modulator (SLM), in which the patterned SLM retardation is translated into a spatial pattern of polarization directions.[9–11] These techniques have been used for the fabrication of flat LC-based optical components with very high optical efficiency, such as polarization gratings, geometric phase lenses, holograms and multi-twist retarders.[12–15] These components are either made on a single substrate, by polymerizing one or multiple thin spin-coated LC layers, or as a LC cell in which the top- and bottom substrate are illuminated with the same alignment pattern. An interesting situation is obtained when top and bottom substrates are illuminated with different planar photo-alignment patterns, because this allows the formation of more complex LC configurations.[16–22] The frustration when the azimuthal angles for corresponding locations at top and bottom substrate are different, can often be resolved by a position-dependent twist in the bulk. For certain combinations of alignment patterns however, the topology at the interfaces requires either the creation of a disclination line along which the director is undefined, or a line along which the director is perpendicular to the substrate (homeotropic).[16,17,19,22] For the second case, the line of perpendicular directors usually ends in one or more defects when it reaches the end of the (usually line-shaped) photo-alignment pattern on one of the substrates. In this work we use closed ring-shaped alignment patterns in a uniform background, avoiding the need for defects at the termination of the alignment pattern.

A local disturbance in a vector field that is homogeneous in the far-field can be considered as a soliton. Such solitons have

* Both B.Berteloot and I.Nys contributed equally to this work.

[a] Liquid Crystals & Photonics Group, Department of Electronics and Information Systems, Ghent University, Technologiepark-Zwijnaarde 126,B-9052 Ghent, Belgium. E-mail: brecht.berteloot@ugent.be

[b] Physics of Soft and Partially Ordered Matter theory and simulation group, Department of Physics, University of Ljubljana, Jadranska 19, 1000 Ljubljana, Slovenia.

† Electronic Supplementary Information (ESI) available: Video of the effect of focusing with parallel polarizers rotated at 45° and additional images. See DOI: 10.xxx/xxxxxxxxxxxxxx/

View Article Online
DOI: 10.1039/D0SM00308E

been realized in ferromagnetism and in LCs. The group of Smalyukh has extensively studied nematic and chiral nematic LC solitons that are formed under influence of vortex beams in a LC cell with homeotropic alignment at both substrates.[23–25] The resulting topological structures with or without disclinations, identified as torons or hopfions, can be stable, although homeotropic alignment in the bulk has a lower elastic energy. The structures studied by the Ozaki group[22,26] can also be considered as solitons.

In this work we design a confined photo-alignment pattern on one substrate and combine it with homogeneous alignment at the second substrate. In the ring-shaped photo-alignment pattern the azimuthal angle increases from zero at the inner radius to 360° at the outer radius (fig. 3). Inside the inner radius, and outside of the outer radius, the alignment direction is equal to the rubbing direction at the top substrate. We show that this complex alignment pattern, in which the director near the substrates remains planar, can generate a defect-free 3D director configuration that contains a closed ring in which the director is perpendicular to the substrate. Because the director at a distance from the center is the same on both substrates, the structure can be considered as a topological soliton that is cut in half by the substrate with the photo-alignment pattern.[23] We show that the same photo-alignment pattern can also give rise to three other structures: one with two disclination rings, one with a single disclination ring and a 180° twist in the center, and one with a 360° twist in the center of the ring. In their experiments Sunami et al. use a similar circular photo-alignment pattern, but with only a 180° rotation of the azimuthal angle and therefore they find only one structure with a single disclination ring.[26] In the following we discuss the technology for the fabrication process, the patterned alignment and the cell assembly, show polarization optical microscopy (POM) images of the structures, present finite-element Q-tensor simulations for the director configuration and corresponding transmission simulations based on a beam propagation method (BPM).

2 Cell fabrication

The fabrication procedure of the LC cell is shown in fig. 1. The cell is based on two cleaned glass substrates which have an indium tin oxide (ITO) coating that functions as a transparent electrode. On one of the substrates, a Nylon film is spin-coated (3500 rpm, 45 s) (fig. 1 (a)). After drying the film in the oven for 4 hours at 180 °C, the planar alignment is defined by rubbing a velvet cloth over the Nylon coating (fig. 1 (b)).

The second glass substrate defines the local LC orientation through patterned photo-alignment. The ITO coated surface of this substrate is cleaned by an ozone-plasma treatment for 15 minutes. The photo-alignment layer, composed of 0.2 wt% Brilliant Yellow (BY) in dimethylformamide (DMF) is prepared and spin-coated onto the treated substrate (3000 rpm, 30 s) (d). Both the BY and DMF are purchased from Sigma-Aldrich. After spin-coating, the sample is put onto a hotplate for 5 minutes at 90 °C. This substrate is exposed to the projected SLM image to define the pattern of the photo-alignment layer (e). By moving the sample between subsequent illuminations, multiple patterns can be written next to each other (f).
To define the cell thickness, spacers with a diameter of 5.5 μm

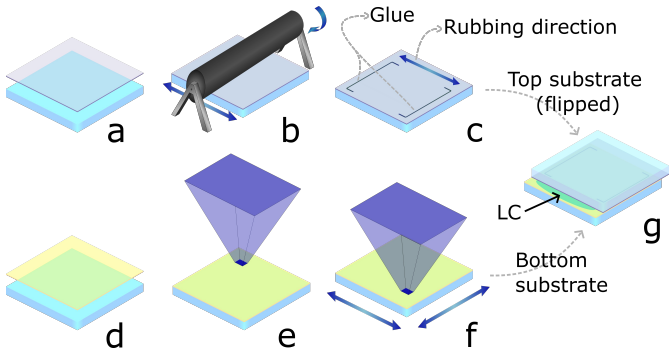

Fig. 1 Fabrication process for the liquid crystal cell.

are mixed with the glue (NOA68) that is applied on the edges of one substrate (c). The two samples are pressed together and the glue is cured by ultraviolet (UV) illumination. The exact cell thickness is then measured through interferometry. This is done on multiple locations of the cell to estimate the uniformity. After the thickness is measured, the sample is heated to 80 °C and filled with nematic LC (E7).

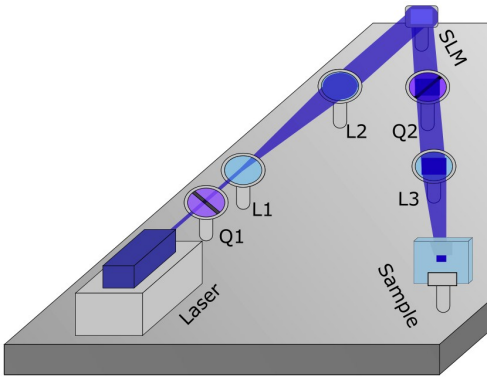

Fig. 2 Setup for the patterned photo-alignment, with a blue laser a spatial light modulator (SLM), 2 quarter-wave plates Q1-Q2 and 3 lenses L1-L3.

The patterned photo-alignment is realized by an optical setup with a blue laser and a SLM. The setup is shown in fig. 2. The blue laser (Cobolt Twist, 200 mW, $\lambda = 457$ nm) emits vertically polarized light that is converted into circular polarization by a quarter-wave plate Q1. Lenses L1 and L2 form a beam expander so that the full surface of the SLM is illuminated. The SLM (Holoeye Pluto-2) has a pixel pitch of 8 μm and a resolution of 1920 by 1080 pixels. The SLM uses a parallel aligned nematic LC panel and modulates the phase of the horizontal polarization component. The magnitude of the modulation depends on the voltage that is applied to the corresponding pixel. This voltage is encoded by the grey scale (0-255) in the displayed image (fig. 3). Quarter-wave plate Q2 converts the phase modulation into a rotation of the linear polarization. When linearly polarized light is incident on the photo-alignment layer, the LC will orient perpendicularly to the local orientation of the linear polarization. The projection of the SLM can be scaled up or down by changing the position of the projection lens L3.

For the definition of the rings in the photo-alignment layer, the

View Article Online
DOI: 10.1039/D0SM00308E

pattern shown in fig. 3(a) is displayed on the SLM. The grey level of the background and in the central area of each ring aligns the LC director parallel to the x-direction. The LC on the rubbed substrate is also aligned along the x-direction. A rotation of 360° of the azimuthal anchoring angle ϕ is defined between the inner- and the outer radius of the ring:

$$\begin{aligned} \phi &= 0 \;\; for \;\; r < r_{in} \\ \phi &= 2\pi \frac{r - r_{in}}{r_{out} - r_{in}} \;\; for \;\; r_{in} < r < r_{out} \\ \phi &= 0 \;\; for \;\; r_{out} < r \\ with \;\; r_{in} &= 20\,\mu m \;\; and \;\; r_{out} = 50\,\mu m \end{aligned} \tag{1}$$

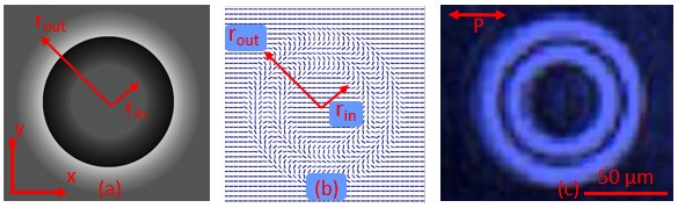

Fig. 3 Gray scale pattern written on the SLM. Each grey level corresponds to an azimuthal angle (a). Resulting LC alignment profile (b). CCD image of the inhomogeneous illumination after passing through a polarizer (c).

The resulting LC alignment is shown in fig. 3(b). By replacing the sample with a linear polarizer and a CCD camera, the resulting modulated polarization pattern can be observed (fig. 3(c)). The dimensions of the rings are defined by the number of pixels in the SLM image and by the magnification of the projection. In our experiments the inner- and outer radii of the rings are r_{in}=20 μm and r_{out}=50 μm. The distance D between the centers of neighboring rings is 120 μm in both x- and y-direction (fig. 5). We only investigated square lattices of rings in this manuscript, but other types of lattices (with higher packing density) can equally be tested.

3 Measurements

Once the heated sample is completely filled with LC, the cell is cooled down to room temperature. Using the uniform ITO coatings of the glass substrates, an electric field is generated perpendicular to the glass substrates. A voltage of 10 V_{pp} is applied and the LC aligns perpendicularly to the glass substrates (vertically) in the bulk of the cell. Close to the substrates however, the LC follows the planar alignment defined by the alignment layers. The transmission profile between crossed polarizers is expected to be bright when the LC at the photo-patterned substrate is oriented at azimuthal angle ϕ ±45°, ±135°, ±225° or ±315°. The four bright lines in fig. 4(a) confirm that there is indeed a 360° rotation of the LC at the surface. Because this retardation is rather small, the microscope illumination was increased to make the transmission profile more visible in fig.4(a). When the polarizer and analyzer are rotated over 45° with respect to the x- and y-axis, two dark rings are visible (fig. 4(b)). The planar anchoring direction at the top (rubbed) substrate is parallel to the x-axis. When the anchoring direction at the bottom substrate is parallel to the y-axis, the retardation created near the top- and bottom substrate are subtracted and the transmission remains dark. When the anchoring direction at the bottom substrate is also parallel to the x-axis, the retardations are added and the transmission is brighter.

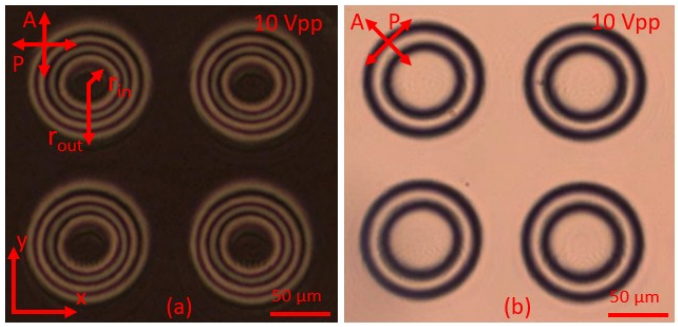

Fig. 4 Microscope images of the cell with a voltage of 10 V_{pp} applied. The transmission is shown for the cell between crossed polarizers aligned with x- and y-axes (a) and for crossed polarizers rotated over 45° with respect to the x- and y-axes (b).

After the voltage is decreased to 0 V, the images in fig. 5 are obtained. With polarization optical microscopy (POM) the ring-shaped structure is visible, even in the absence of polarizers. We will refer to this director configuration as structure A. Note that in each image the color observed in the center of the rings is the same as the color of the background.

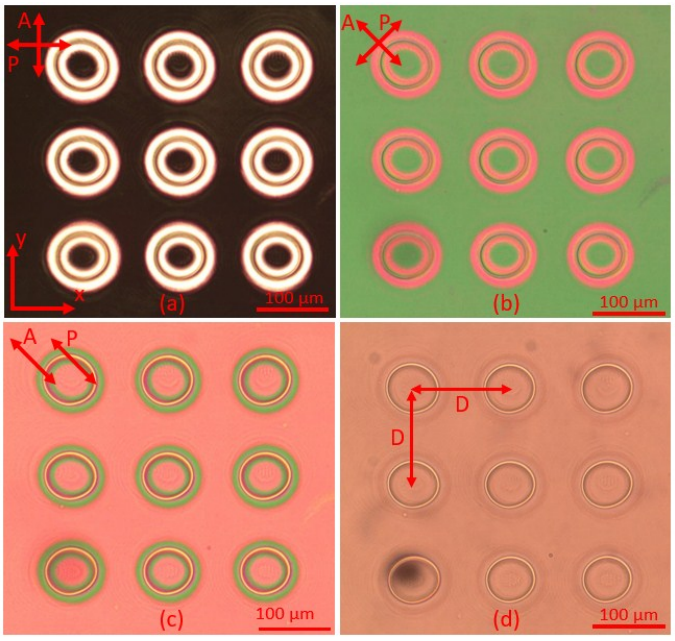

Fig. 5 Microscope images of structure A at 0 V between crossed polarizers (a), crossed polarizers rotated 45° with respect to the x- and y-axes, with parallel polarizers rotated 45° (c) and without polarizers (d).

When the device is heated to the isotropic state and cooled down without any voltage applied, a different structure is often observed as illustrated in figure 6(b). In this case a circular discli-

View Article Online
DOI: 10.1039/D0SM00308E

nation line is observed with radius closer to the outer radius of the photo-patterned ring. We will refer to this configuration as structure B. Note that for structure B the color observed in the center of the ring by optical polarization microscopy is different from the color of the background.

Figure 6(c) shows a third structure that is sometimes observed in our patterned sample (0V, room temperature). We will refer to this configuration as structure C. Structure C is, in contrast to structures A and B, usually not achieved immediately but after leaving the sample at room temperature without an applied voltage for several hours. In the POM images where the polarizers are rotated 45° with respect to the x- and y-axes, the color changes continuously with the radius and also here the color observed in the center of the ring is different from the color of the background.

The fourth structure that was only occasionally observed, is shown in fig. 6(d). We will refer to this configuration as structure D. Two ring-shaped disclination lines are visible and the center of the ring has again the same color as the background.

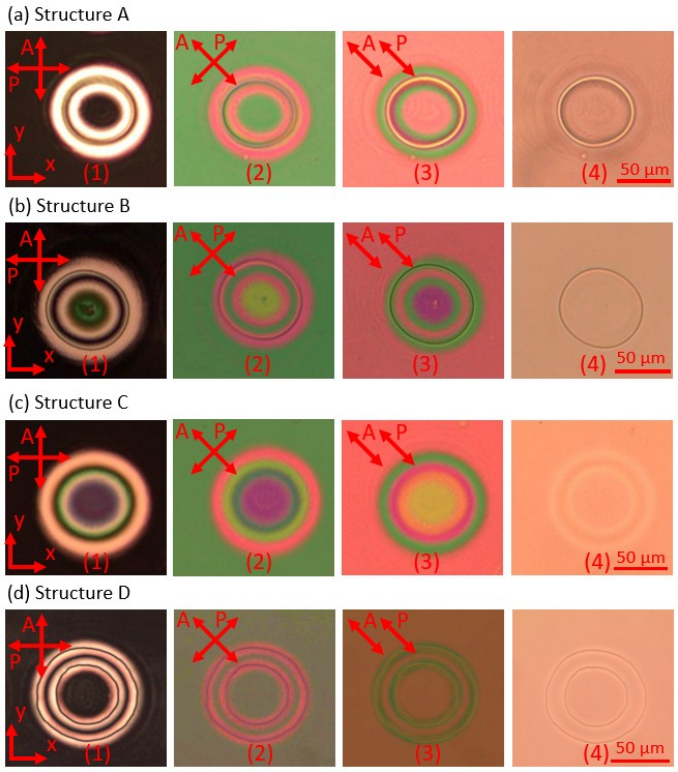

Fig. 6 Microscopy images for structures A, B, C and D, for different orientations of the polarizer and analyser.

The relative occurrence of the structures A, B, C and D was varying in different tested samples and was depending on the moment of observation and the history of the sample. Shortly after a voltage cycle, structure A is usually observed, while structure C is often dominant after leaving the sample at room temperature for several hours. Structure B on the other hand was regularly observed after cooling down the sample from the isotropic state to room temperature without applied voltage.

In figures 3-6 all photo-alignment patterns consist of rings with the same rotation direction, the same size (r_{in} and r_{out}) and distance D between neighbouring centers. In the following we varied the pattern on the SLM, to define different LC photo-alignment patterns.

A first variation is shown in figure 7 where the distance D between the centers of the rings is 100 μm (instead of 120 μm) and neighboring rings touch each other (D = 2 r_{out}). With a voltage of 10 V_{pp} applied to the LC layer, the alignment at the photo-aligned substrate is analyzed (fig. 7(c)). Once the voltage is gradually decreased to 0 V structure A is recovered (fig. 7(d)), and the interaction with neighboring rings is also minimal for this alignment configuration. For the alignment with touching rings, also structures B, C and D were achieved. Microscope images of this are given in fig. S1 and S2 of the supplementary information.

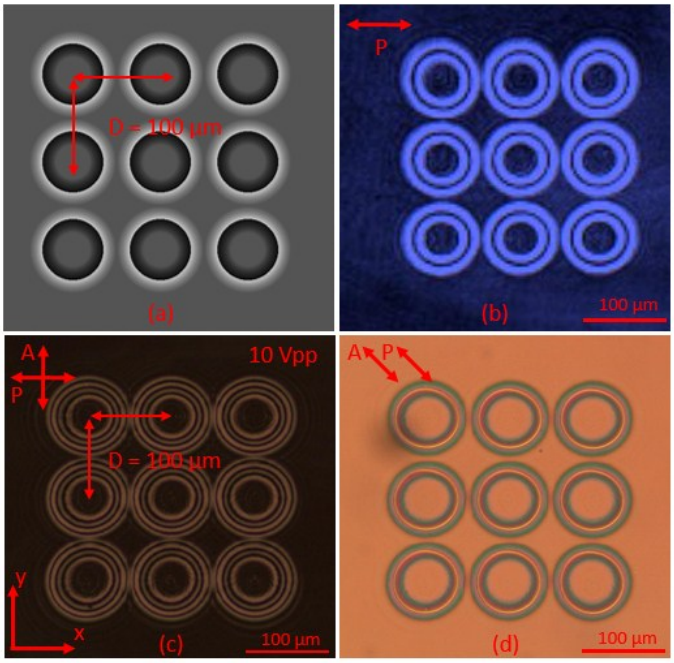

Fig. 7 Gray scale pattern written on the SLM when the spacing D = 2 r_{out} (a). CCD image of this illumination after passing through a polarizer (b). Microscope images between crossed polarizers when a voltage of 10 V_{pp} is applied (c) and between 45° rotated parallel polarizers at 0 V.(d)

The second variation is shown in figure 8. The rings on odd locations (1, 3, 5, 7, 9) define a rotation of the LC that is opposite to the one defined in equation 1:

$$\phi = -2\pi \frac{r - r_{in}}{r_{out} - r_{in}} \quad for \;\; r_{in} < r < r_{out} \qquad (2)$$

$$with \;\; r_{in} = 20\,\mu m \;\; and \;\; r_{out} = 50\,\mu m$$

It can be seen in figures 8 (b, c, d) that the radius of these five rings (1, 3, 5, 7, 9) slightly differs from the other four rings (2, 4, 6, 8), which is due to non-idealities in the photo-alignment setup. Apart from that, rings with opposite rotation direction show very similar behavior.

In the supplementary information, microscope images for a ring unit with r_{in} = 66 μm and r_{out} = 93 μm are shown (fig. S3). For this larger ring, only structures A and B were observed.

View Article Online
DOI: 10.1039/D0SM00308E

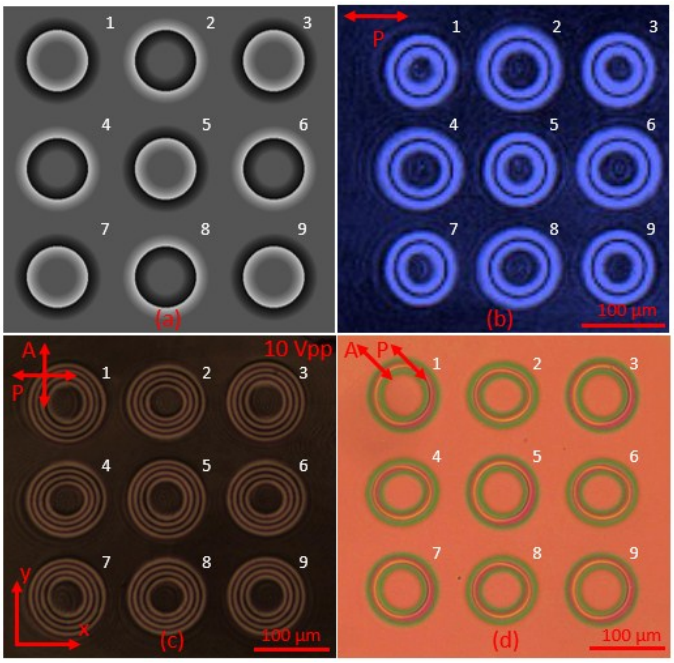

Fig. 8 Gray scale pattern written on the SLM when the rotation direction is opposite for all odd elements (1, 3, 5, 7, 9) (a). CCD image of this illumination after passing through a polarizer (b). Microscope images between crossed polarizers when a voltage of 10 V_{pp} is applied (c) and between 45° rotated parallel polarizers at 0 V.(d)

Adjusting the dimensions r_{in} and r_{out}, changes the stability of the different structures, but the topology is maintained.

4 Simulations

To identify the director configuration in the experimentally observed structures A, B, C and D, FE simulations are performed. By combining FE Q-tensor simulations for the director configuration with optical simulations, direct comparison between the experimental POM images and the simulation results can be obtained.

The LC director simulations are performed with a self-implemented code developed in collaboration with University College London.[27,28] The FE Q-tensor simulation model makes use of a minimization of the Landau-de-Gennes (LDG) free energy F_{LDG} to find the equilibrium director configuration:[27–30]

$$F_{LDG} = \int_{\Omega} f_d + f_{th} + f_e \, d\Omega + \int_{\Gamma} f_s \, d\Gamma \qquad (3)$$

with f_d the elastic distortion energy density, f_{th} the thermotropic (or Landau) energy density, f_e the external electric field induced energy density and f_s the surface energy density appearing at interfaces. The different energy contributions are expressed in terms of the order tensor Q. The description of the LC director with a symmetric tensor (Q-tensor) instead of a vector allows to model disclinations and local variations in the order parameter. The order parameter can freely vary in the vicinity of the defect core but deviation from the equilibrium order parameter gives rise to a contribution to the thermotropic bulk energy term f_B:

$$f_B = \frac{A}{2} tr(Q^2) + \frac{B}{3} tr(Q^3) + \frac{C}{4} tr(Q^2)^2 \qquad (4)$$

For the bulk thermotropic coefficients we use:

$$A = -2 * 0.87 * 10^2 \frac{N}{m^2}$$

$$B = -2.12 * 10^3 \frac{N}{m^2}$$

$$C = 1.74 * 10^3 \frac{N}{m^2}$$

giving rise to an equilibrium order parameter of 0.54 at a reduced temperature of -2°C. The addition of a thermotropic bulk energy term is based on a phenomenological model and is an extension of the original theory of Oseen, Frank and Zocher.[31–33] It allows for variations in the order parameter and the simulation of disclination lines without singularities in the free energy density. The thermotropic parameters A, B, C can be linked to experiments by fitting equation 4 to experimentally obtained data of order parameter variations with respect to the temperature. These type of experiments are not reported for E7 and in general the theory is only strictly applicable close to the transition temperature (to describe features of the phase transition). To get a qualitative description, we used values for the thermotropic coefficients based on the experimentally measured values for 5CB.[34] As is common in the literature, we use values for the thermotropic coefficients that are a few orders of magnitude smaller than the experimentally measured ones.[28,35] This increases the length scale of variations in the order parameter and allows to obtain faster numerical convergence.

The alignment conditions at the top and bottom interfaces are assumed to be strong and in the simulations the LC director is therefore fixed at the substrates (last term in equation 3 disappears). Uniform planar alignment parallel to the x-axis and with a pretilt angle of 2° (w.r.t. the xy-plane) is imposed at the top surface. At the bottom surface the pretilt angle is 0° and the azimuthal anchoring angle is varying as defined in equation 1 with r_{in} = 20 μm and r_{out} = 50 μm. A unit cell with dimension D* D * d = 120 μm * 120 μm * 5.5 μm is simulated and periodic periodic boundary conditions are applied in the x- and y-direction. The elastic and dielectric properties of the LC E7 are used in the simulation (K_{11} = 11.1 pN, K_{22} = 6.5 pN, K_{33} = 17.1 pN, $\varepsilon_{\perp}$ = 5.2 and $\varepsilon_{\parallel}$ = 19.0). The elastic constants K_{11}, K_{22} and K_{33} do not appear in the Q-tensor description of the elastic distortion energy

View Article Online
DOI: 10.1039/D0SM00308E

f_d but they can be linked to the coefficients L_1, L_2 and L_6:

$$f_d = \frac{1}{2}L_1 Q_{\alpha\beta,\gamma}Q_{\alpha\beta,\gamma} + \frac{1}{2}L_2 Q_{\alpha\beta,\beta}Q_{\alpha\gamma,\gamma} + \frac{1}{2}L_6 Q_{\mu\gamma}Q_{\alpha\beta,\mu}Q_{\alpha\beta,\gamma}$$

with

$$L_1 = \frac{1}{27S_{\text{eq}}^2}(K_{33} - K_{11} + 3K_{22})$$

$$L_2 = \frac{2}{9S_{\text{eq}}^2}(K_{11} - K_{22})$$

$$L_6 = \frac{2}{27S_{\text{eq}}^3}(K_{33} - K_{11})$$

$$S_{\text{eq}} = \frac{-B + \sqrt{B^2 - 24AC}}{6C} \tag{5}$$

Different metastable states, corresponding to local minima in the free energy, can be identified by imposing different starting configurations in the simulation tool. In this way we were able to identify the director configurations in the experimentally observed structures A, B, C and D. As an example, initial conditions that are suited to simulate structure A, B, C and D are shown in the supplementary information (fig. S4). By imposing appropriate initial conditions we were able to simulate the four experimentally observed structures, in addition, starting from other initial conditions did not yield other stable structures.

Comparison of the free energy of the different director configurations, with and without disclination lines present, is inaccurate. A continuum description of defects is possible within the Landau-de Gennes theory by taking into account a thermotropic energy contribution. The size of this contribution to the free energy is however not well-defined, especially far away from the transition temperature (as is the case for E7 at room temperature) and for LC materials as E7 for which the thermotropic coefficients are not experimentally determined.[36] We do not aim to make a quantitative comparison between the free energy of the different structures, but use the simulations tool to get a good qualitative description of the possible LC configurations in the device.

A tetrahedral volume mesh is used to simulate the 3D director configuration and the results are interpolated on a regular grid to perform the optical simulations. The optical simulations rely on the open-source software *Nemaktis* (`https://github.com/warthan07/Nemaktis`) developed by one of us (G.P.). Shortly, optical fields are propagated through the LC sample using a generalized beam propagation method[37] allowing to recast Maxwell equations for birefringent media in a simpler Schrödinger-like equation of the type $\partial_z \boldsymbol{E}_\perp = i\mathbf{L}\boldsymbol{E}_\perp$ for the transverse field $\boldsymbol{E}_\perp$. This includes a dominant contribution to the phase evolution similar to the Jones method[38] supplemented by a diffraction operator fully including the anisotropy of the permittivity tensor and a walk-off operator taking into account the tilt between the Poynting vector and the wavevector (both of which were given partially in some specific systems[39,40] but were never obtained for general birefringent media). The focusing optics of the microscope, whose numerical aperture is 0.2, is taken into account in the simulation using well-known formula of Fourier optics[41]. Color images are simulated by taking a CIE illuminant A for the light source and projecting the spectrum of the transmitted microscope images on the sRGB color space. The dispersion of the ordinary and extraordinary refractive index of E7 are taken into account using the Cauchy formula:

$$\begin{aligned} n_e &= 1.67906 + \frac{0.01546\,\mu m^2}{\lambda^2} + \frac{0.001663\,\mu m^4}{\lambda^4} \\ n_o &= 1.49669 + \frac{0.00785\,\mu m^2}{\lambda^2} + \frac{0.00026\,\mu m^4}{\lambda^4} \end{aligned} \tag{6}$$

The simulated director configurations for the four different structures A, B, C and D are represented in figure 9. The corresponding simulated microscopy images for different orientations of the polarizer and analyser are summarized in figure 10. The color in fig. 9 represents the twist angle with respect to the x-axis. Remark that 90° and -90° twist are equivalent thanks to the non-polar symmetry of the LC director.

Since the different structures contain a very non-uniform director configuration with strong spatial variations, diffraction effects will be present and will influence the observed microscopy images. Adjusting the focus of the microscope also has an important effect on the observed image. A video in which the microscope focuses at varying distances can be found in the supplementary information. The optical simulation tool allows to simulate this effect and as an example some simulated microscopy images for structure A at a different focus are shown in fig. 11. Simulation results for a cell thickness of 5.5 μm and 6 μm are combined in this figure to illustrate also the influences of the cell thickness. Figure 11 demonstrates that focusing and exact cell thickness play an important role when making a detailed comparison between simulated results and experiments.

5 Discussion

In the design that we have proposed, the director outside of the outer ring and the director on the homogeneously aligned substrate are both along the x-direction. If the LC between the two substrates is considered together with its mirror image with respect to the bottom substrate, the resulting structure can be considered as a topological soliton. To achieve the soliton condition, we have to neglect the pretilt of a few degrees at the top substrate. The photo-alignment pattern on the bottom substrate can therefore be considered as the generator of three-dimensional solitons in the bulk. The vector field of a soliton can be represented by the 3D director pattern, but there are also alternative representations, for example by pre-images (a pre-image is formed by a set of points with the same director).[23–25] The pre-images for zero tilt for example are circles on the bottom substrate in our configuration.

Below we discuss the four different LC structures that are created based on the same photo-alignment pattern. Two of them are of particular interest, because the director is continuous (without any singular disclinations).

View Article Online
DOI: 10.1039/D0SM00308E

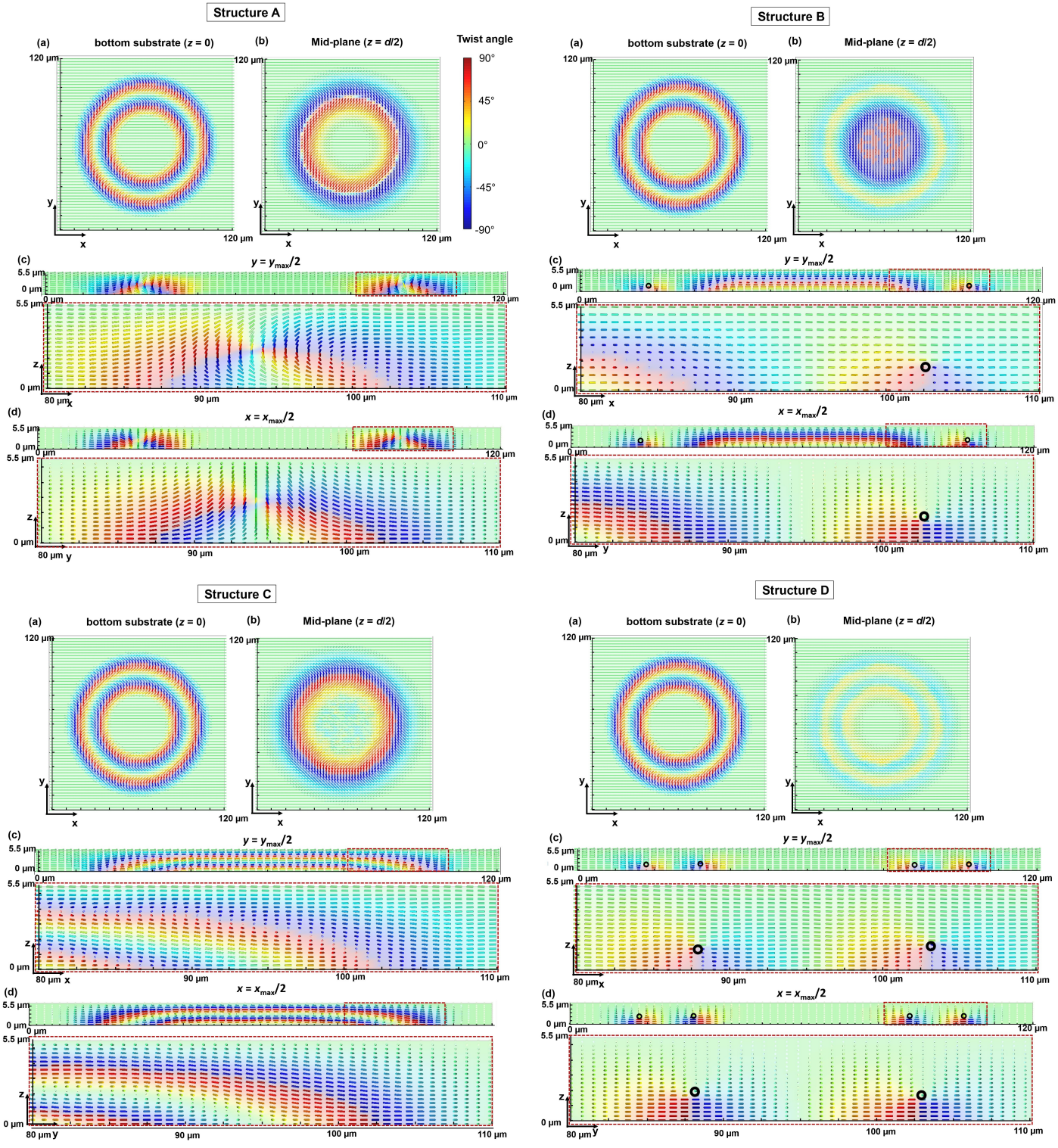

Fig. 9 Simulated director configuration for structure A (top left), B (top right), C (bottom left) and D (bottom right) without applied voltage. The color represents the twist angle with respect to the x-axis. The director configurations at the bottom substrate (a), in the mid-plane z = d/2 (b), and in two perpendicular cross-sections y = y_{max}/2 (c) and x = x_{max}/2 (d) are shown. The defects in the director configuration are indicated by a black circle.

View Article Online
DOI: 10.1039/D0SM00308E

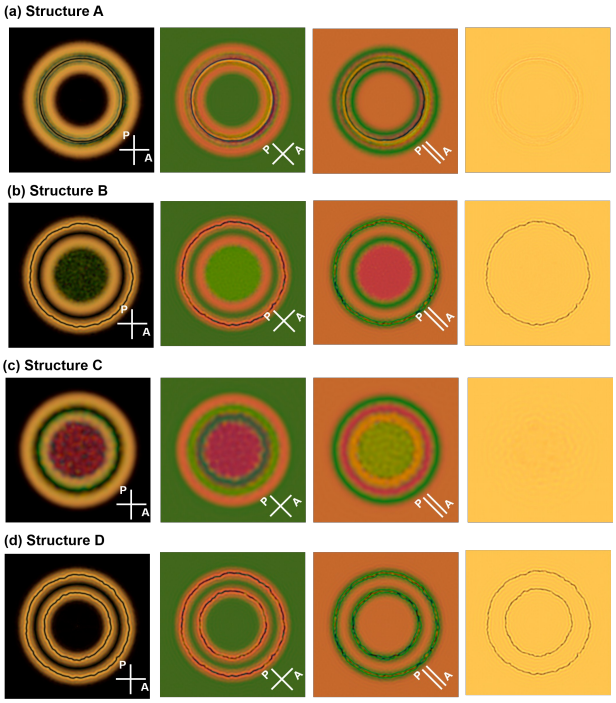

Fig. 10 Simulated microscopy images for structures A, B, C and D, for different orientations of the polarizer and analyser (in focus).

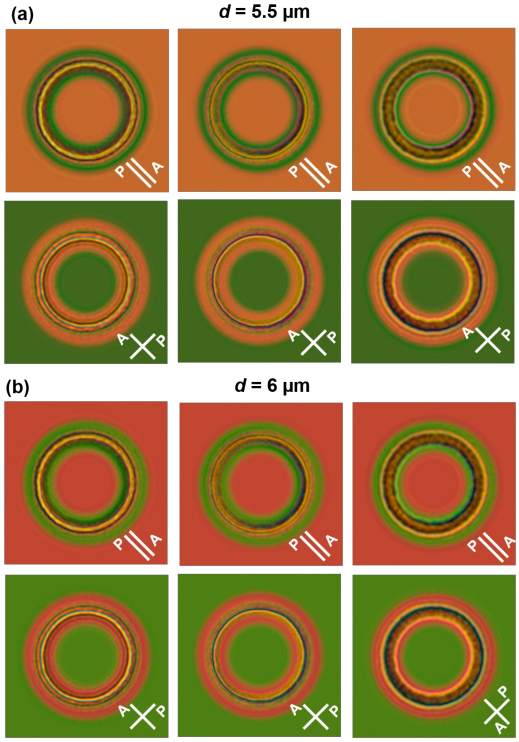

Fig. 11 Simulated microscopy images for structure A between crossed polarizers (rotated 45° with respect to the x- and y-axis), for different focus and for different cell thickness.The cell thickness is 5.5 μm and 6 μm in (a) and (b) respectively. The focus distance is -20 μm, 0 μm and 20 μm from left to right.

Structure A

It is clear that the experimental POM images in fig.5 and the simulated transmission simulations in fig.10(a) agree very well. Small differences between the two can be attributed to uncertainty in the cell thickness and to focusing effects. As can be seen in fig. 11, the match between the POM images and the simulated transmission profile is the best for the focus distance chosen as -20 μm. The pink and green background observed under 45° rotated polarizers with respect to the x- and y-axis, match better for the simulated configuration with cell thickness 6 μm (fig. 11 (b)).

The cross sections of the simulated director configuration (fig. 9 (a)) indicate that structure A contains a ring along which the LC director aligns perpendicular to the substrates. A similar out-of-plane director orientation in the bulk due to patterned photo-alignment on both substrates has been observed by Nys et al. [16,17] In essence, this localized out-of-plane orientation of the LC director allows to avoid twist-disclinations due to conflicting surface anchoring conditions at the confining substrates. The absence of singularities in the director structure agrees with the fact that no disclination lines are observed in the POM images. For structure A the pre-images (regions with identical director) are closed rings, that slightly deviate from the circular shape, due to the dissimilarity of the three elastic constants (figure 12). There is one closed ring (roughly half way between the top and the bottom substrate, with radius between r_{in} and r_{out}) for which the alignment is along the z-axis (figure 12).

Structure B

Comparison between the experimental POM images in fig. 6(b) and the simulated transmission profiles in fig. 10(b) yields good agreement. The simulated transmission profile also displays two green-colored rings, with a thin black disclination line on top of the outer green ring. The center ($r < r_{in}$) is also pink, and different from the background color ($r > r_{out}$).

The simulated cross sections in fig. 9 (b) show that in the inner region ($r < r_{in}$), where the alignment direction at top and bottom substrates are identical, the LC director remains practically planar and makes a 180° right-handed twist. The sense of twist is defined by the sense of rotation in the photo-patterned ring. The 180° twist is the cause of the color change in the central area $r < r_{in}$.

Apart from the twist in the center of the ring, there is also a singular disclination line in structure B, with radius $r \approx r_{in} + 3(r_{out} - r_{in})/4$. Near the middle of the photo-patterned ring ($r = r_{in} + (r_{out} - r_{in})/2$), there is a region where the director remains practically parallel to the x-axis, independent of the z-coordinate. In the optical transmission images, this region has the same color as the outer background $r > r_{out}$.

Structure C

The POM images for structure C in fig. 6 (c) show a strong agreement to the simulated transmission profiles of fig. 10(c). The simulated cross sections of this structure (fig. 9 (c)) show that in the inner region ($r < r_{in}$), where the alignment direction at the top and bottom substrate is parallel, the LC director remains close to planar, making a 360° right-handed twist around the z-axis. In

View Article Online
DOI: 10.1039/D0SM00308E

the region between the inner and the outer ring, the helical axis is tilted away from the z-axis. In this way, the handedness of the twist corresponds to the the rotation direction defined in the photo-patterned ring. There are no disclination lines in this structure but a chiral bulk structure is created in the achiral LC cell. We can conclude that for the given photo-alignment pattern, it is possible to avoid singular disclinations not only by an out-of-plane reorientation of the LC director in the bulk (as in structure A) but also by introducing a 360° twist in the inner region of the ring (as in structure C). The pre-images for structure C are more complex than for structure A. They either consist of two separated closed curves, or of one single closed curve (figure 12). In structure C the maximum tilt angle is 15° and the pre-image curve reduces to a point when the tilt angle is increased to this maximum value.

Structure D

Finally also the agreement between the experimentally observed POM images for structure D (fig.6(d)) and the simulated transmission profiles (fig. 10(d)) is obvious. The simulated director configuration (fig. 9 (d)) shows the appearance of two singular disclination loops near $r \approx r_{in} + (r_{out} - r_{in})/4$ and $r \approx r_{in} + (r_{out} - r_{in}) * 3/4$ which are also obtained in the transmission images. In the inner region of the photo-patterned ring ($r < r_{in}$) and near the middle of the ring ($r \approx r_{in} + (r_{out} - r_{in})/2$), the alignment at the top- and bottom substrate is the same and the director remains more or less uniform in the bulk of the cell and the observed color is similar to the unpatterned background.

Based on the alignment pattern, the formation of structure D with two disclination loops could be expected, in particular for cells with small thickness. In our experiments structure D is not often observed, because there are possibilities to avoid the disclination loops (structure A and C).

6 Conclusions

We have shown that the combination of a substrate with uniform planar alignment and a substrate with a ring of rotating photo-alignment, leads to the formation of different LC configurations in the bulk of the cell. Even though the alignment patterns at the top and bottom substrates define planar alignment with conflicting azimuths, bulk configurations without singular disclinations are observed. In total four different structures, with or without twist disclination lines, have been experimentally observed and numerically simulated. In the most simple configuration (structure D) two disclination loops are formed to resolve the twist conflict at the confining substrates. In our ring-shaped photo-alignment configuration with 360° rotation, disclination lines can be avoided by introducing a twist deformation in the bulk of the achiral LC. One disclination line can disappear by inducing a 180° twist in the central region (structure B) or both disclination lines can disappear by introducing a 360° twist in the central region (structure C). On the other hand, the need for discontinuities in the director configuration can also be avoided by creating a ring with vertical director orientation in the bulk (structure A). The twist elastic energy is high in structure C; there is an important energy cost associated with the disclination lines in structures B

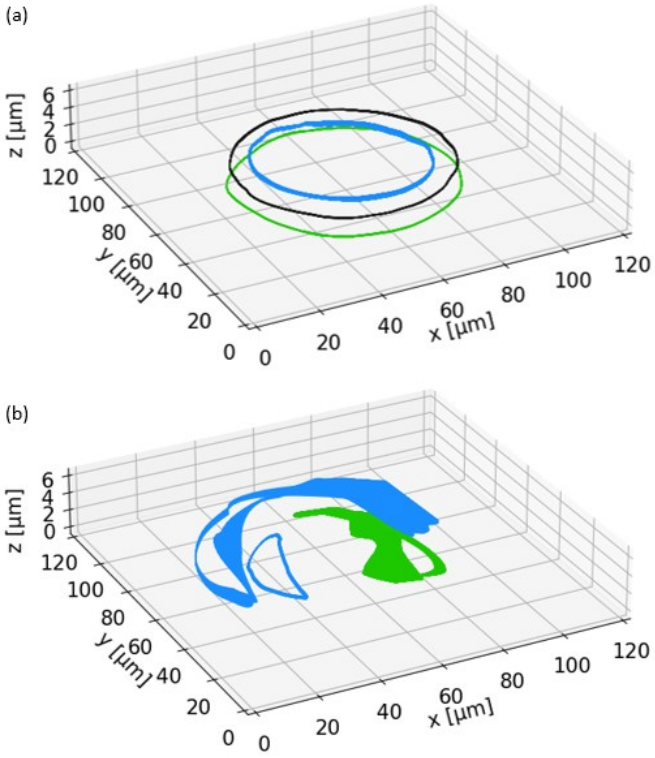

Fig. 12 3D view of pre-images, showing points with identical director. Pre-images for structure A (a), for vertical director orientation (tilt angle θ = 90°, black); for ϕ=-45°, θ =10° (blue); and for ϕ=0°, θ = -10° (green). Pre-images for structure C (b), ϕ=-45°, θ = 5 ° (blue); ϕ=0 °, θ = -5° (green).

View Article Online
DOI: 10.1039/D0SM00308E

and D, while structure A has considerable splay and bend energy. The relative weight of the different energy contributions and the stability of the different structures does not only depend on the LC that is used but also depends on the geometric parameters r_{in}, r_{out} and d. The configuration that is studied here (r_{in} = 20 μm, r_{out} = 50 μm and d = 5.5 μm) allows to observe all four structures and is interesting to study metastability. This system however offers a rich playground to develop different LC devices and one of the structures could for example be favored by changing the geometric parameters or by adding some chirality to the nematic LC material.

Small well-defined multistable periodic structures can find applications in displays with low energy consumption (one bright state and one dark state), smart windows (one scattering state and one clear state),or multistable microlenses (one lensing state and one neutral).

Conflicts of interest

There are no conflicts to declare.

Acknowledgements

The authors would like to acknowledge funding from the Flemish Agency for Innovation and Entrepreneurship through grant HBC.2017.0554, from the ARRS (Javna Agencija za Raziskovalno Dejavnost RS) through grant P1-0099 and from the European Union's Horizon 2020 program through the Marie Skłodowska-Curie grant agreement No. 834256 and European Topology Interdisciplinary Action (EUTOPIA CA17139).

References

1 X. Xiang, J. Kim and M. Escuti, *Scientific Reports*, 2018, **8**, 7202.
2 X. Xiang, J. Kim, R. Komanduri and M. Escuti, *Optics Express*, 2017, **25**, 19298–19308.
3 E. Shteyner, A. Srivastava, V. Chigrinov, H.-S. Kwok and A. Afanasyev, *Soft Matter*, 2013, **9**, 5160–5165.
4 Y. Guo, M. Jiang, C. Peng, K. Sun, O. Yaroshchuk, O. lavrentovich and Q.-H. Wei, *Advanced Materials*, 2016, **28**, 2353–2358.
5 K. Gao, C. McGinty, H. Payson, S. Berry, J. Vornehm, V. Finnemeyer, B. Roberts and P. Bos, *Optics Express*, 2017, **25**, 6283–6293.
6 T. Zhan, J. Xiong, Y.-H. Lee, R. Chen and S.-T. Wu, *Optics Express*, 2019, **27**, 2632–2642.
7 M. Miskiewicz and M. Escuti, *Optics Express*, 2014, **22**, 12691–12706.
8 J. Kim, Y. Li, M. Miskiewicz, C. Oh, M. Kudenov and M. Escuti, *Optica*, 2015, **2**, 958–964.
9 J. Davis, D. McNamara, D. Cottrell and T. Sonehara, *Applied Optics*, 2000, **39**, 1549–1554.
10 L. D. Sio, D. Roberts, Z. Liao, S. Nersisyan, O. Uskova, L. Wickboldt, N. Tabiryan, D. Steeves and B. Kimball, *Optics Express*, 2016, **24**, 18297–18306.
11 Y. Li, Y. Liu, S. Li, P. Zhou, T. Zhan, Q. Chen, Y. Su and S.-T. Wu, *Optics Express*, 2019, **27**, 9054–9060.
12 S. Serak, D. Roberts, jeoung Yeon Hwang, S. Nersisyan, N. Tabiryan, T. Bunning, D. Steeves and B. Kimball, *Journal of the Optical Society of America B*, 2017, **34**, B56–B63.
13 X. Xiang, J. Kim and M. Escuti, *Crystals*, 2017, **7**, 383.
14 R. Komanduri, J. Kim, K. Lawler and M. Escuti, *Proc. SPIE Emerging Liquid Crystal Technologies*, 2012, **7**, 82790E.
15 I. Nys, M. Stebryte, Y. Y. Ussembayev, J. Beeckman and K. Neyts, *Advanced Optical Materials*, 2019, **7**, 1901364.
16 I. Nys, J. Beeckman and K. Neyts, *Soft Matter*, 2015, **11**, 7802–7808.
17 I. Nys, J. Beeckman and K. Neyts, *Soft Matter*, 2018, **33**, 6892–6902.
18 G. Crawford, *Journal of Applied Physics*, 2005, **98**, 123102.
19 M. Honma, W. Toyoshima and T. Nose, *Journal of Applied Physics*, 2016, **120**, 143105.
20 M. Honma, K. Takahasi, R. Yamaguhi and T. Nose, *Japanese Journal of Applied Physics*, 2016, **55**, 041701.
21 M. Honma and T. Nose, *Optics Express*, 2012, **20**, 18449–18458.
22 T. Ouchi, K. Imamura, K. Sunami, H. Yoshida and M. Ozaki, *Physical Review Letters*, 2019, **123**, 097801.
23 J.-S. B. Tai, P. Ackerman and I. Smalyukh, *Proceedings of the national Academy of Sciences*, 2018, **115**, 921–926.
24 I. Smalyukh, Y. Lansac, N. Clark and R. Trivedi, *Nature materials*, 2010, **9**, 139–145.
25 P. Ackerman and I. Smalyukh, *Physical Review X*, 2017, **7**, 011006.
26 K. Sunami, K. Imamura, T. Ouchi, H. yoshida and M. Ozaki, *Physical Review E*, 2018, **97**, 020701.
27 R. James, E. Willman, F. A. Fernandez and S. E. Day, *IEEE Transaction on Electron Devices*, 2006, **53**, 1575–1582.
28 E. Willman, F. A. Fernandez, R. James and S. E. Day, *IEE Journal of Display Technology*, 2008, **4**, 276–281.
29 P. G. de Gennes and J. Prost, *The Physics of Liquid Crystals*, Clarendon Press, 1993, pp. 76–78.
30 L. D. Landau, E. M. Lifshitz and L. P. Pitaevskii, *Statistical Physics*, Pergamon Press, 1980, pp. 440–442.
31 C. Oseen, *Trans. Faraday Soc.*, 1933, **29**, 883–889.
32 F. C. Frank, *Disc. Faraday Soc.*, 1958, **25**, 19–28.
33 H. Zocher, *Trans. Faraday Soc.*, 1933, **29**, 945–957.
34 H. J. Coles, *Molecular Crystals and Liquid Crystals*, 1978, **49**, 67–74.
35 L. A. Parry-Jones and S. Elston, *Journal of Applied Physics*, 2005, **97**, 093515.
36 Y. Deng-Ke and W. Shin-Tson, *Fundamentals of Liquid Crystal Devices*, John Wiley |& Sons, Ltd, 2015, pp. 13–18.
37 G. Poy and S. Žumer, *in writing*, 2020.
38 M. Schubert, C. Cramer, J. A. Woollam, C. M. Herzinger, B. Johs, H. Schmiedel and B. Rheinländer, *Journal of the Optical Society of America A*, 1996, **13**, 1930.
39 C. Conti, M. Peccianti and G. Assanto, *Physical Review E*, 2005, **72**, 066614.
40 Q. Wang, G. Farrell and Y. Semenova, *Journal of the Optical Society of America A*, 2006, **23**, 2014.

View Article Online
DOI: 10.1039/D0SM00308E

41 J. W. Goodman, *Introduction to Fourier optics*, Roberts and Company Publishers, 2005.

View Article Online
DOI: 10.1039/D0SM00308E

Graphical Abstract figure:

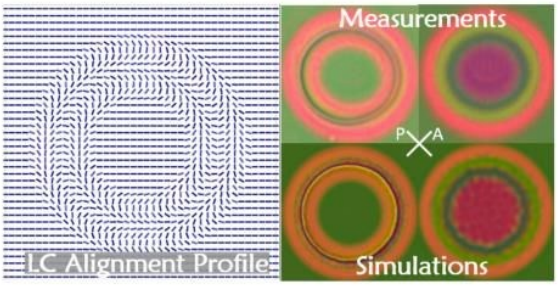

Text:

Ring-shaped planar photo-alignment at the surface gives rise to different 3D liquid crystal configurations in the bulk.